FOSSEE CFD-OpenFOAM Semester Long Internship Spring 2026

on

'Control and Flow Reaction in a Microfluidic Network'

Mohit Kumar Saw

Mechanical Engineering Department
Visvesvaraya Technological University, Belagavi

Guided by:
Prof. Sameer Jadhav
Department of Chemical Engineering
Indian Institute of Technology

Mentored by:
Pranay Kumar Pandey
FOSSEE, Indian Institute of Technology Bombay

May 2026

Abstract

This investigation analyses the flow behavior in microfluidic channels with rectangular objects over a Reynolds number range of 0.1 and 200. Unsteady, incompressible laminar analysis was carried out using the icoFoam solver from OpenFOAM v2412 software with structured grid generation through the blockMesh tool. The analysis was done on two types of channels, namely the single-object channel and the multi-object channel. Velocity and pressure distribution profiles are provided at Re = 0.1 and Re = 200. At low Reynolds number value, a direct proportionality between pressure and flow is observed. However, at Re = 200, fluid inertia results in the formation of recirculation zones and non-linear Forchheimer-type flow resistance.

Table of Contents

List of Tables

List of Figures

List of Equations

1. Introduction

1.1 Background of the Topic

Microfluidics is a branch of science that studies the control of the transport of fluids through micro-sized channels. These fluids are comprised of particles that range between a few microns to a few hundred microns in size. In light of this fact, the flow is laminar, and the drop in pressure is directly proportional to the rate of flow as per the Hagen-Poiseuille equation. This restriction means that other laws of fluid dynamics cannot be applied.

The area has seen a lot of advancement in the last twenty years, from rudimentary one channel devices to advanced systems combining mixing, separation, reactions, and detection in a single device. But there has remained a continuing problem of having to use external devices like pumps, valves, and pressure regulators to effect flow switching. The realization of a totally integrated system of flow control based only on fluid mechanics has been a goal of many researchers.

1.2 Motivation

It must be pointed out that Case et al. (2019) made a significant breakthrough through incorporating arrays of rigid cylindrical structures into one branch of the five-segment H-network microfluidic system. This allows for the manifestation of nonlinear pressure-flow dynamics that help create direction-dependent flow switching, and the appearance of Braess's paradox – the paradox when the removal of one of the connection conduits leads to an increase in the flow rate. All these effects can be expressed mathematically using the Forchheimer equation. They emerge due to inertial forces generating nonlinearity in the flow resistance regime even with low Reynolds numbers.

Deekshith K. (2025)'s PhD dissertation at IIT Bombay under the guidance of Prof. Sameer R. Jadhav is a comprehensive study which recreates and expands on the experiments carried out by Case et al. (2019), employing OpenFOAM in the process. This internship project will seek to further explore this topic of research and attempt to replicate their results and expand it to the H-network, illustrating flow switching.

1.3 Problem Statement

The major objective of the current study is the identification of the characteristics of the flow velocity and pressure field using the transient Computational Fluid Dynamics (CFD) modeling approach with OpenFOAM v2412, where the effects of the cylindrical objects placed inside the straight microchannel will be analyzed depending on the Reynolds number. The current research will be centered around the analysis of the following objects:

(a) Contours of velocity and pressure distribution for one cylindrical object for Re = 0.1 and Re = 200.

(b) Contours of velocity and pressure distribution for multiple objects for Re = 0.1 and Re = 200.

(c) Time-dependent profiles of flow rate and pressure drop for all four cases under consideration.

1.4 Literature Review

The governing physics of microfluidic flows were established through foundational studies on low-Reynolds-number flows. At $Re \ll 1$, inertia is negligible and the Stokes equations adequately describe the velocity field. As Re increases into the intermediate laminar range ($Re \sim 10–1000$), inertial forces generate flow separation and recirculation in the lee of bluff bodies, introducing nonlinearity into the overall pressure–flow relationship.

The nonlinear resistance behaviour of arrays of obstacles was described rigorously by the Forchheimer equation, which extends Darcy's law with a quadratic term in flow velocity. This quadratic correction captures the increasing importance of inertial losses through porous-like structures at higher flow rates. For cylindrical obstacles in a microfluidic channel, the Forchheimer equation takes the form $-\Delta P = \alpha\mu LV + \beta\rho LV^2$, where V is the mean velocity and α, β are geometric constants.

Case et al. (2019) published the pivotal experimental and computational demonstration that Braess's paradox can manifest in microfluidic networks containing obstacle-laden channels. They showed that, above a critical inlet pressure, the flow direction through a linking channel reverse and that closing the linking channel at those pressures actually increases total network flow rate. This counter-intuitive effect is made possible by the nonlinear resistance of the obstacle-laden channel.

Deekshith K. (2025) systematically explored the hydraulic resistance of single and multiple stacks of rectangular obstacles in 2D and 3D microchannels using OpenFOAM, quantified the dependence of the Forchheimer coefficients on obstacle geometry, and investigated the microfluidic Wheatstone bridge network. The velocity and pressure data from those simulations serve as validation benchmarks for the present work.

2. Governing Equations

All simulations in this study solve the unsteady, incompressible Navier–Stokes equations in two dimensions. The fluid is assumed to be Newtonian and the flow laminar throughout.

Continuity equation (Equation 1):

$$\nabla \cdot u = 0$$

This enforces mass conservation, requiring the velocity field to be divergence-free for an incompressible fluid.

Navier–Stokes momentum equation (Equation 2):

$$\partial u/\partial t + (u \cdot \nabla)u = -(1/\rho)\ \nabla p + \nu\ \nabla^2 u$$

In this equation, u is the velocity vector [m/s], p is the kinematic pressure (p/ρ) [m^2/s^2], ρ is the density of the fluid [kg/m^3], and $\nu=\mu/\rho$ is the kinematic viscosity [m^2/s]. In the left side of the equation, the total acceleration is given. While on the other side, there is the pressure gradient and the diffusion term due to viscosity. Convection $(u \cdot \nabla)u$ creates inertial forces that can be neglected only for low Reynolds number flows.

Reynolds number (Equation 3):

$$Re = U \cdot w / \nu$$

where U denotes the velocity at the inlet [m/s], and w denotes the channel width [m]. Reynolds number measures the ratio of inertial forces to viscous forces. If $Re < 1$, then flow is in the creeping flow (Stokes flow), and the pressure-flow curve is linear. In this range of $10 \le Re \le 300$ (as considered in the current study), flow is nonlinear due to inertia but remains laminar.

Hagen–Poiseuille relation for a straight channel (Equation 4):

$$-\Delta P = (12\mu L / w^3) \cdot Q$$

The relation, which is straightforward, states that the pressure difference ΔP is directly proportional to the discharge rate per unit depth Q in a uniform rectangular cross section channel with width w and length L, under the condition that there are no obstacles present and that the Reynolds number is low.

Forchheimer equation for obstacle-laden channels (Equation 5):

$$-\Delta P = (\alpha\mu^2 L / 2\rho w^2)\ Re + (\beta\mu^2 L / 4\rho w^2)\ Re^2$$

In this case, α is referred to as the inverse of permeability while β is the non-Darcy factor. Both are dependent on the geometry of the channel (Case et al., 2019). Due to the quadratic relationship between the Reynolds number and the pressure drop in equation (3), ΔP increases at a faster rate than the flow rate.

3. Turbulence Modelling

Simulations in this study will be performed under laminar flow regime. Reynolds numbers of interest include Re = 0.1 and Re = 200, which do not exceed turbulence onset (generally Re > 2300 for pipe flow but lower, but above several hundreds, for channel flows having bluff bodies inside). Laminar flow is sustained for cylinder located between parallel walls till Reynolds number of approximately Re = 200 – 300 depending on blockage ratio.

As a result, there is no turbulence modeling involved. Simulation Type should be set to laminar in constant/turbulenceProperties dictionary. Direct Navier-Stokes solution will be used without averaging and eddy viscosity modeling. It is justified because this way of solving problem corresponds to that used in Case et al. (2019) and Deekshith K. (2025) who validate this choice for current Reynolds number range.

4. Computational Domain

4.1 Geometry

Two straight channel configurations network are studied. All geometries are two-dimensional; the spanwise direction (z) is assigned a single-cell depth with the empty boundary condition.

Single-obstacle channel:

A rectangular channel of length 9.5 mm and width 600 µm contains a single rectangular obstacle of height 570 µm placed at the channel centerline at x = 2 mm from the inlet. The obstacle spans the full depth of the 2D domain. The channel dimensions follow those reported by Deekshith K. (2025).

Multi-obstacle channel:

The same rectangular domain is modified to include three rectangular obstacles of the same height arranged in a collinear array along the centerline, equally spaced between x = 2 mm and x = 2.618 mm with obstacle 6 µm width. Increasing the number of obstacles enhances the cumulative Forchheimer nonlinearity, as demonstrated by Case et al. (2019).

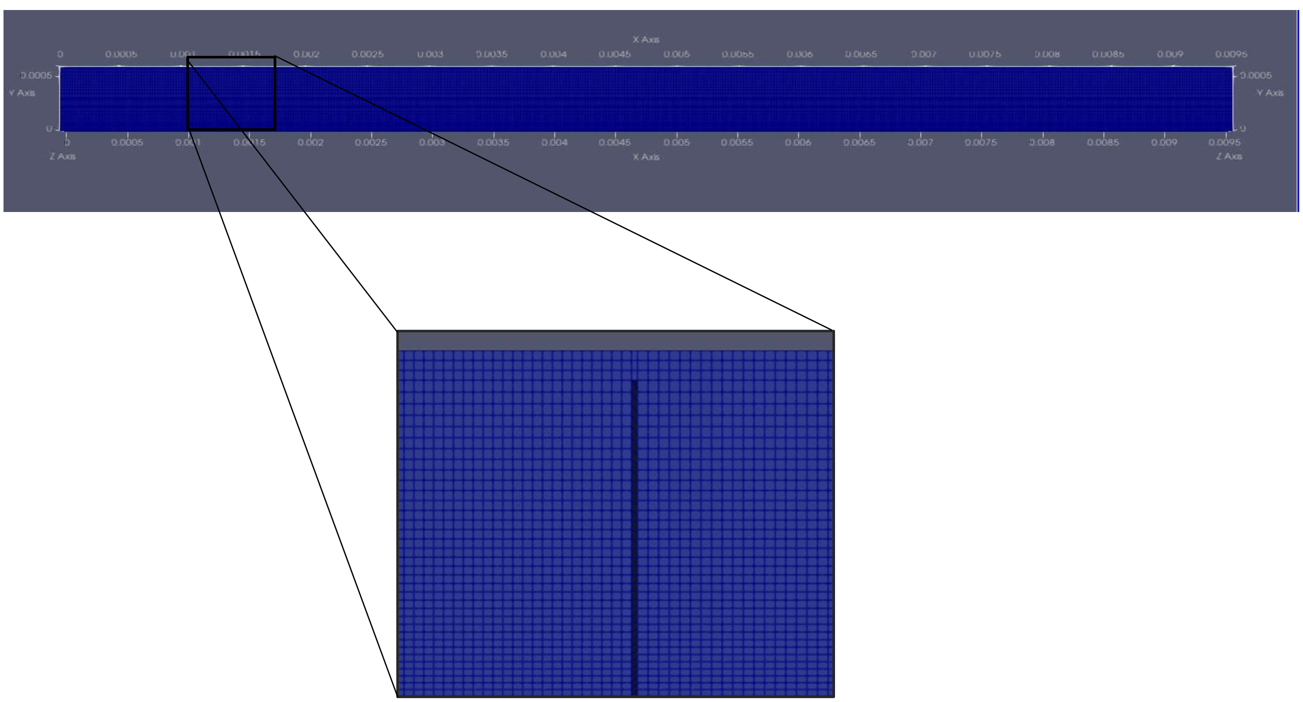

Figure 1 – blockMesh geometry for the single-obstacle channel (full view and obstacle-region zoom)

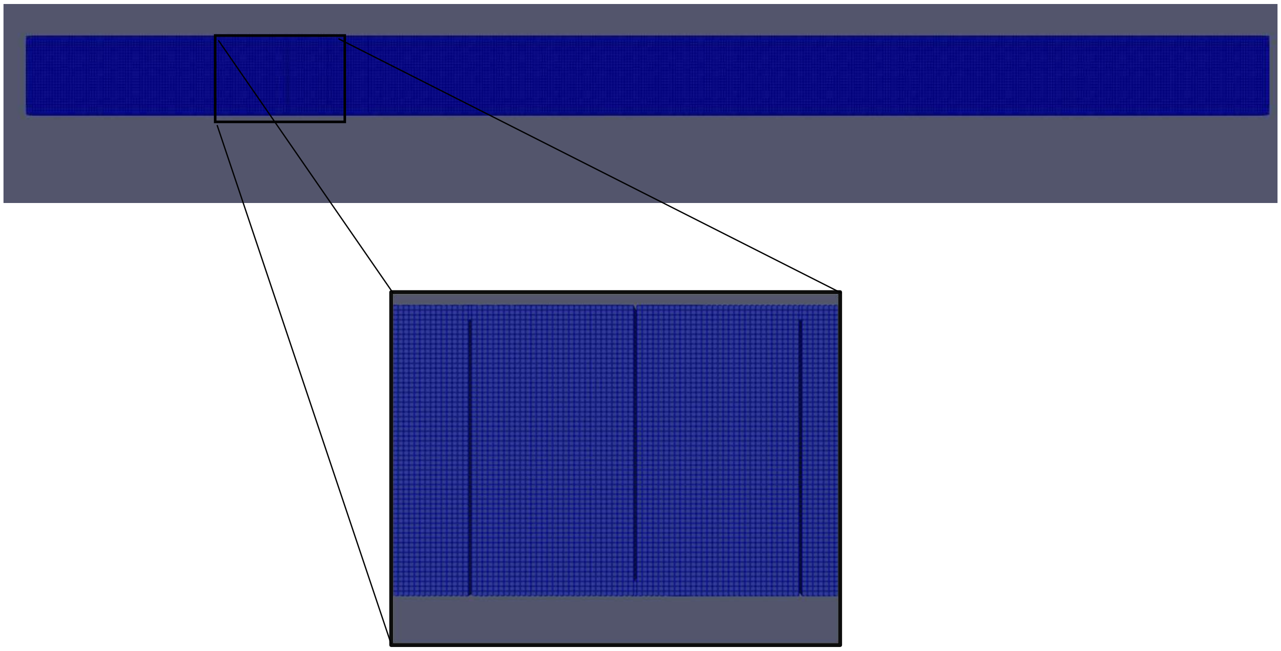

Figure 2 – blockMesh geometry for the multi-obstacle channel (full view and obstacle-region zoom)

4.2 Mesh

Structured hex meshes are created using the blockMesh tool available in OpenFOAM 2412. Multi-block method is used to fit the mesh around the obstacle boundaries without deviating from the Cartesian grid pattern. Mesh is refined around the obstacle to handle the expected sharp gradients of velocity and pressure.

For the single-obstacle flow, the total number of cells is around 15,000, with the cell aspect ratio close to one in the proximity of the obstacle. In the case of the multi-obstacle flow, the number of cells is about 40,000, which is required for the proper representation of the wake interaction process. The uniform cell size of 25 µm x 25 µm is used around the obstacle area. At the moment, no mesh sensitivity analysis is performed.

4.3 Boundary and Initial Conditions for All Parameters

The boundary and initial conditions are identical across all four simulation cases. Table 1 and Table 2 summarize these settings.

Table 1 – Initial Conditions

Flow Variable	Value
Velocity U	0 m/s
Pressure p	0 m^2/s^2

Table 2 – Boundary Conditions

Patch	U Condition	U Value	p Condition
inlet	fixedValue	(U 0 0) m/s	zeroGradient
outlet	inletOutlet	0 m/s	fixedValue 0
walls	noSlip	0 m/s	zeroGradient
obstacle	noSlip	0 m/s	zeroGradient
frontAndBack	empty	—	empty

The inlet velocity U is set to achieve the target Reynolds number using Re = Uw/ν. With w = 600 µm and ν = 10^{-6} m²/s (water): U = 1.666666667e-04 m/s for Re = 0.1 and U = 0.3333 m/s for Re = 200. Note: kinematic viscosity ν = 10^{-6} m²/s is fixed as for water at 20 °C, and U is varied.

4.4 Solver Selection

The transient cases are carried out using icoFoam solver. icoFoam is an unsteady and incompressible laminar flow solver that uses the pressure-velocity coupling approach and is incorporated in OpenFOAM. This solver makes use of the PISO (Pressure Implicit with Splitting of Operators) scheme to handle pressure velocity coupling at each time-step. The PISO scheme consists of two corrector steps in each time-step, and therefore yields a second-order temporal accuracy for well-resolved cases.

4.5 Discretization Schemes

The spatial and temporal discretization schemes are specified in the system/fvSchemes dictionary. The schemes selected are listed in Table 3.

Table 3 – Discretization Schemes

Term	Scheme
∂/∂t (temporal)	backward (2nd order, bounded)
∇ (gradient)	Gauss linear
∇· (divergence)	Gauss linearUpwind grad(U)
∇² (Laplacian)	Gauss linear corrected
Interpolation	linear

4.6 Simulation Parameters (Re, Co, Δt)

Key simulation parameters for each case are listed in Table 4.

Table 4 – Simulation Parameters

Case	Re	U [m/s]	Δt [s]	End time [s]
Single obstacle	0.1	1.666666667×10^{-4}	1×10^{-5}	0.05
Single obstacle	200	0.3333	1×10^{-5}	0.05
Multi-obstacle	0.1	1.666666667×10^{-4}	1×10^{-5}	0.05
Multi-obstacle	200	0.3333	1×10^{-5}	0.05

The Courant number $Co = U \cdot \Delta t/\Delta x$ was kept below 0.5 throughout all simulations. With $\Delta x \approx 25$ µm and $\Delta t = 1 \times 10^{-5}$ s, $Co \approx 0.8$ at $Re = 200$, which satisfies the stability requirement for the explicit convective term.

5. Implementation in OpenFOAM

5.1 Case Setup Structure

Each OpenFOAM case follows the standard directory structure required for submission to the FOSSEE repository:

```
CaseName/
    0/           (initial and boundary conditions: U, p)
    constant/    (mesh, turbulenceProperties, transportProperties)
    system/      (controlDict, fvSchemes, fvSolution, blockMeshDict)
    Allrun       (shell script to execute blockMesh and icoFoam)
    Allclean     (shell script to remove all generated files)
    README       (case description and run instructions)
```

5.2 Control Dictionary

Temporal properties of the problem are described in the system/controlDict file. Important setups are:

application icoFoam;

startTime 0;

endTime 0.05;

deltaT 1e-5;

writeInterval 0.001 (outputting data every 20 time step);

runTimeModifiable yes.

Also, function objects for measurements are added to the controlDict file. In particular, the fieldAverage function object calculates time-averaged velocity and pressure field, and the surfaceFieldValue function object extracts the information about flow rate and pressure at the inlet and outlet boundaries each time data is saved. Function objects provide the information for plotting flow rate and pressure drop graphs described in the Results section.

5.3 Running Procedure and Total Time

Simulations were done serially (single core) on OpenFOAM v2412. All-run ran blockMesh then icoFoam. Wall-clock times per simulation case were around: ~3 minutes for single obstacle cases; ~8 minutes for multi-obstacle cases. The H channel meshing with blockMesh alone took less than 10 seconds.

Post processing was done using ParaView version 5.11, which comes included in the OpenFOAM v2412 package. Velocity and pressure contour maps were generated using the Surface (with Edges) view type in ParaView. Flow rate and pressure drop time histories were generated using Plot Selection Over Time filter in ParaView.

6. Results and Discussions

6.1 Case 1 – Single Obstacle at Re = 0.1

At Re=0.1, the influence of viscosity is more significant than inertia. The simulation reaches its steady-state condition within the first 0.01 seconds of simulation time and remains relatively unchanged for the rest of the period.

Velocity contours (Figure 3): The velocity profile is fairly smooth and is nearly symmetric relative to the axes parallel to the obstacle. The fluid undergoes a considerable amount of acceleration inside the two thin spaces located between the surface of the obstacle and the boundaries of the channel, achieving a maximum speed of 3.8×10^{-3} meters per second, or almost 19 times greater than the average inflow speed. This acceleration can be attributed to the conservation of mass in the decreased cross-sectional area. The velocity distribution returns to the fully developed Poiseuille type around 1-2 channel widths downstream from the obstacle.

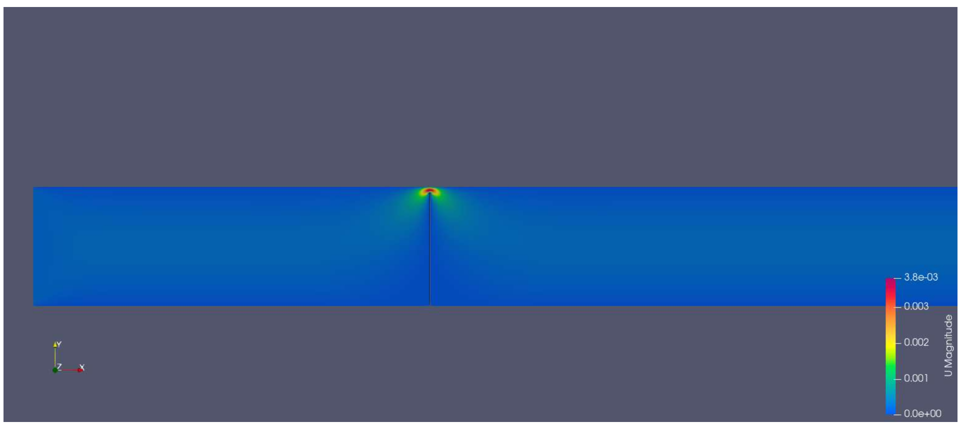

Figure 3 – Velocity magnitude contour, single obstacle, Re = 0.1 (t = 0.033 s)

Pressure Contour (Fig. 4): There exists a well-distributed high pressure upstream of the blockage, followed by a sharp and abrupt drop over the blockage surface. The pressure partially recovers downstream of the blockage to reach the outlet. In general, there is a pressure drop of about 1.8×10^{-3} Pa in the entire channel, which corresponds to the theoretical value as predicted by the Hagen-Poiseuille relation.

Figure 4 – Pressure contour, single obstacle, Re = 0.1 (t = 0.033 s)

It is also observed from Figures 5 and 6 that the flow rate tends to reach a steady value of about 8×10^{-15} m^3 s^{-1} per unit depth after the first few time steps. Similarly, the pressure difference also attains a steady state with very little fluctuation. Thus, the absence of fluctuations is a clear indication of creeping flow.

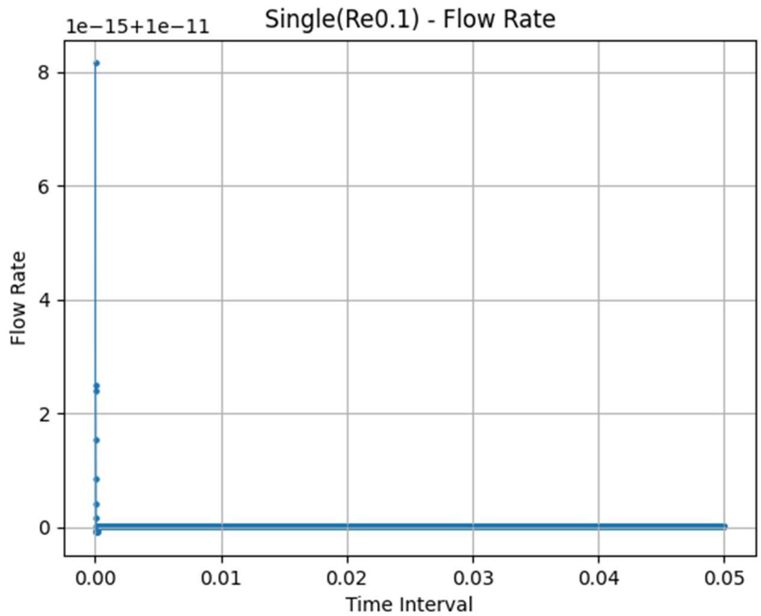

Figure 5 – Flow rate vs. time interval, single obstacle, Re = 0.1

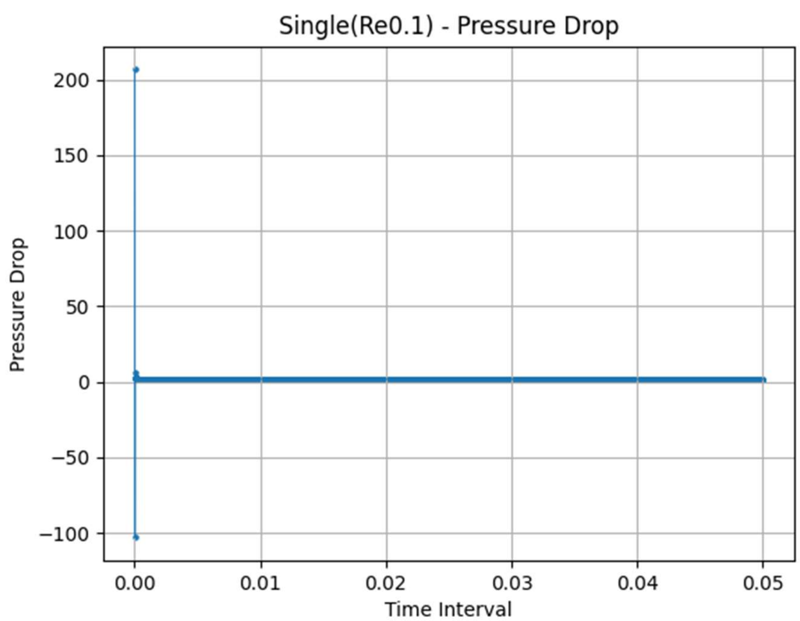

Figure 6 – Pressure drops vs. time interval, single obstacle, Re = 0.1

6.2 Case 2 – Single Obstacle at Re = 200

At Re = 200, inertial forces are no longer negligible. The flow develops transient, oscillatory behaviour that persists throughout the simulation duration.

Velocity contour (Figure 7) The velocity field is very different from the low-Re case. The velocity reaches a maximum of about 9.6 m/s in the gap region, about 24 times the inlet velocity, showing strong acceleration by the constriction. The obstacle motion produces a strong recirculation zone which sheds alternately, producing a von K\'arm\'an-like vortex wake. The wake structure varies in time with the vortices being advected downstream and gradually decayed. This unsteady shedding is the physical basis for the oscillatory flow rate in the time-history plot.

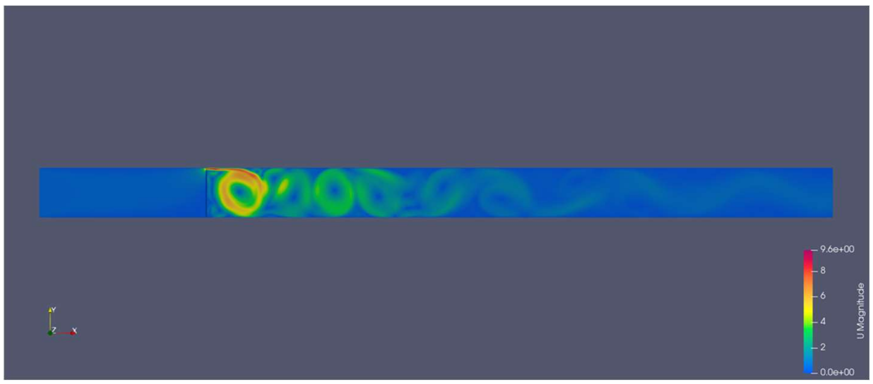

Figure 7 – Velocity magnitude contour, single obstacle, Re = 200 (t = 0.033 s)

Pressure contour (Figure 8): At Re = 200 the pressure drops across the obstacle are of the order of 5.8×10^1 Pa, four orders of magnitude larger than at Re = 0.1, clearly showing the nonlinear amplification of resistance by inertial effects. Immediately behind the obstacle, a region of strongly negative pressure (blue zone) is seen, corresponding to the low-pressure core of the recirculation vortex. This negative pressure feature is characteristic of the Forchheimer regime and absent in the creeping flow case.

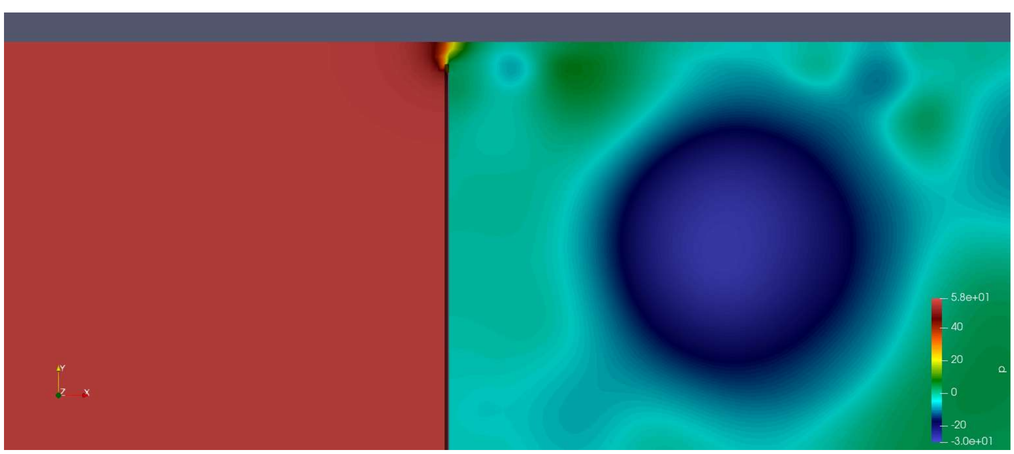

Figure 8 – Pressure contour, single obstacle, Re = 200 (t = 0.033 s)

Time histories (Figs. 9-10): Flow rate shows high-frequency oscillations about a mean of approximately 2.1×10^{-8} m³/s. The amplitude of the oscillation begins at zero and achieves stabilization after t ≈ 0.02 seconds. Pressure difference oscillates about a mean of approximately 5 x 10^4 Pa with a constant amplitude, signifying that the vortex shedding process has become periodic with a limit-cycle behavior. This kind of transient behavior proves the development of inertial effects that are a pre-condition for Forchheimer nonlinearity.

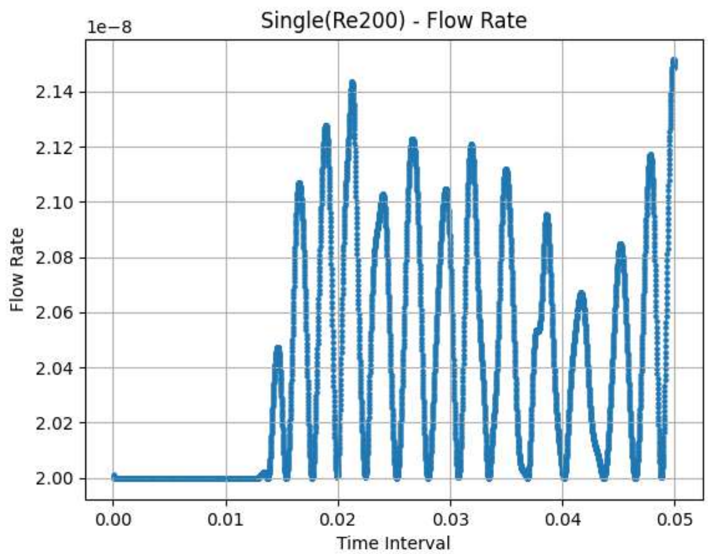

Figure 9 – Flow rate vs. time interval, single obstacle, Re = 200

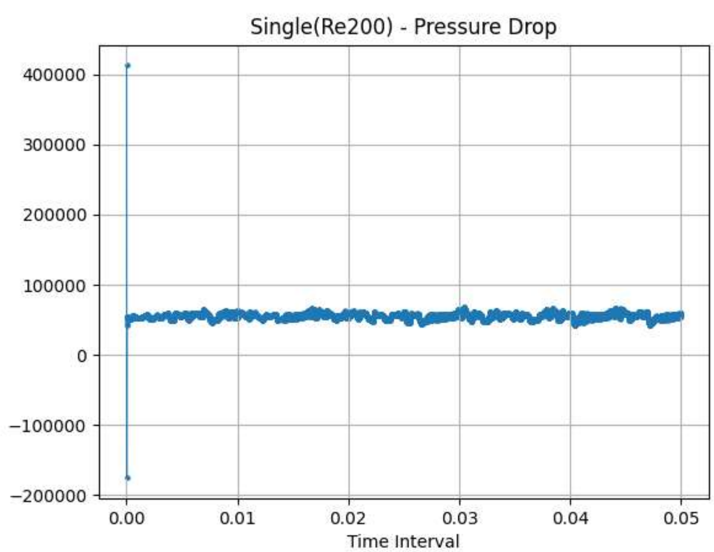

Figure 10 – Pressure drops vs. time interval, single obstacle, Re = 200

6.3 Case 3 – Multi-Obstacle at Re = 0.1

Flow around the multiple obstacles for Re = 0.1 shows the phenomenon of linear superposition of the resistance offered by each obstacle. Pressure drop is achieved independently for each obstacle, and pressure drop within the entire channel increases linearly with respect to the number of obstacles.

Velocity contours: Fluid flow maintains a smooth pattern and symmetry across the entire width of the channel as a result of the low Reynolds number. Acceleration of fluid flow takes place near the narrow openings between the obstacles, where the maximum flow velocity exists. Behind each obstacle, flow velocity decreases steadily without creating any vortex motion or flow separation. It verifies that at Re = 0.1, viscous forces govern flow behavior leading to laminar flow.

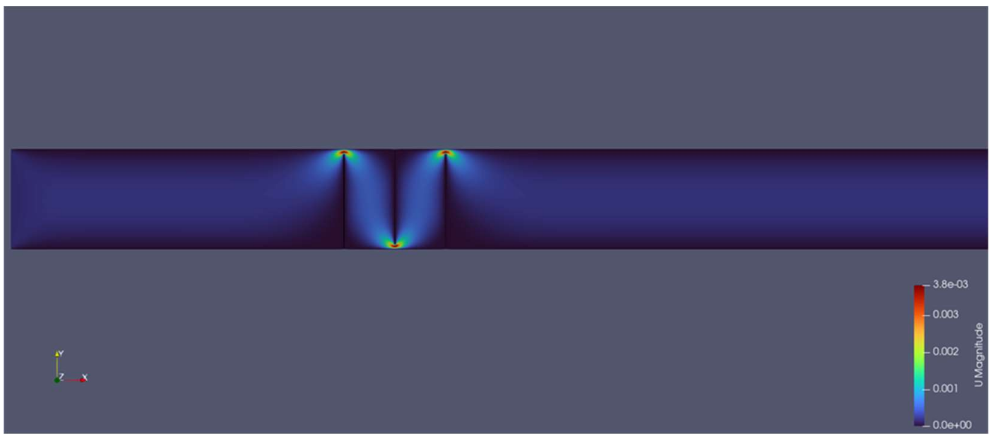

Figure 11 – Velocity contour, multi-obstacle array, Re = 0.1 (t = 0.033 s)

Pressure contour (Figure 12): There is a characteristic stair-like pressure distribution over the channel length, where each step represents the drop in pressure over a particular obstacle. There are three obstacles, which result in equal pressure drops and hence a total pressure drop of about 4.9×10^{-3} Pa, almost 2.7 times greater than the case with just one obstacle – as would be expected with the obstacles being equivalent resistors in series.

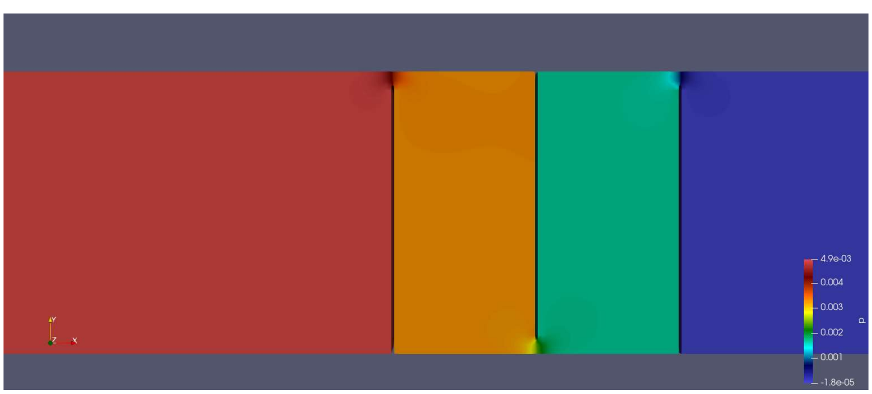

Figure 12 – Pressure contour, multi-obstacle array, Re = 0.1 (t = 0.033 s)

Time histories (Figures 13-14): Both the flow rate and the pressure drop stay constant after a transient start-up period, which means the flow with Re = 0.1 and multi-obstacles is a steady flow. It can be noted that the flow rate with multi-obstacles is almost the same as that with a single obstacle at the same Re value.

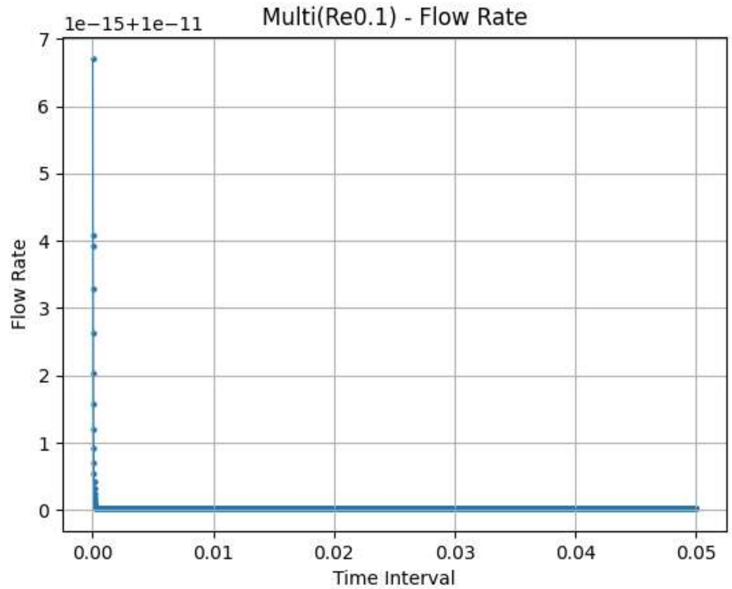

Figure 13 – Flow rate vs. time interval, multi-obstacle, Re = 0.1

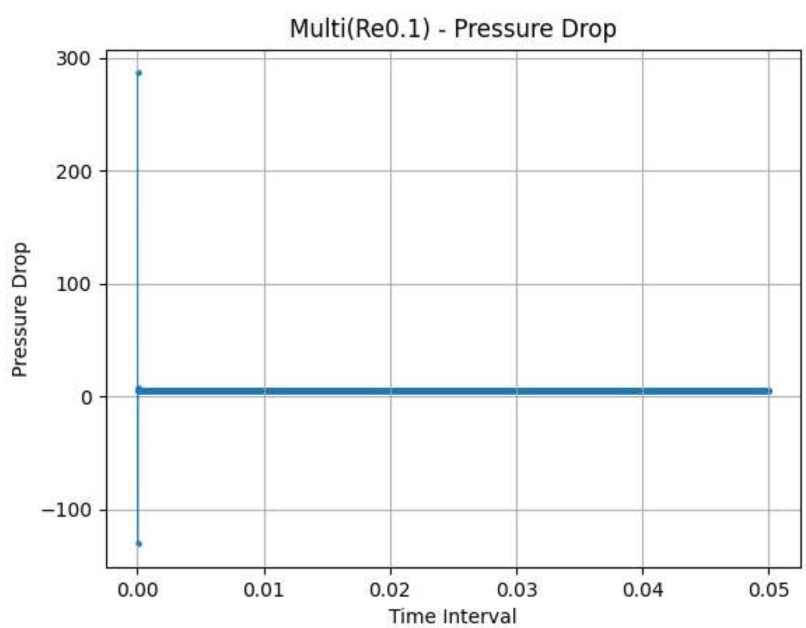

Figure 14 – Pressure drop vs. time interval, multi-obstacle, Re = 0.1

6.4 Case 4 – Multi-Obstacle at Re = 200

Of all the problems investigated, the multi-obstacle problem at Re=200 is the most complicated and physically significant. The effect of the wakes of several obstacles makes for highly nonlinear and dynamically complicated flows.

Velocity contours (Fig. 15): The velocity contour at t = 0.033 s illustrates highly complex interacting wake structures behind each obstacle. Maximum velocities in the gaps (around 10 m/s) are comparable with those in the one obstacle Re=200 problem. However, every subsequent obstacle is subjected to the already disturbed and faster wake of its predecessor, thus intensifying vortex formation behind each post. By the third post, the wake reaches near the whole channel width, and the large-scale recirculation affects the channel walls.

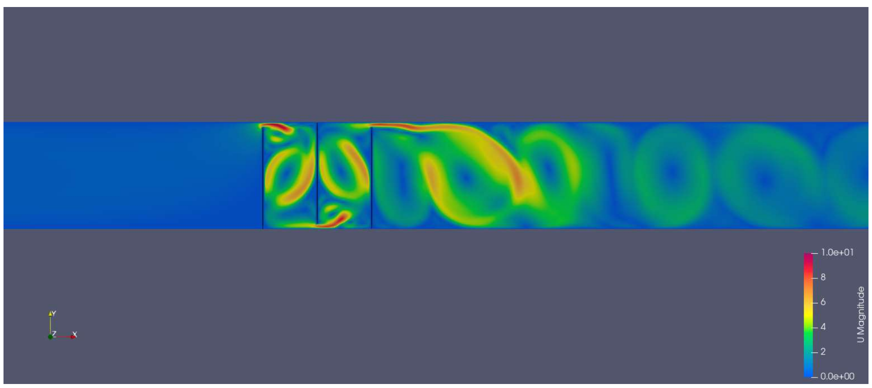

Figure 15 – Velocity magnitude contour, multi-obstacle array, Re = 200 (t = 0.033 s)

Pressure profile (Figure 16): The pressure difference for the channel with three obstacles at Re = 200 is around 1.4×10^2 Pa or nearly 2.4 times the pressure differences for the single-obstacle channels at Re = 200, while three independent resistors would be equal to three times the pressure difference of the single resistor. Such a scaling at higher values of Re is in line with the Forchheimer model in which interactions between wake and obstacle cause effective increase in the resistance of subsequent obstacles.

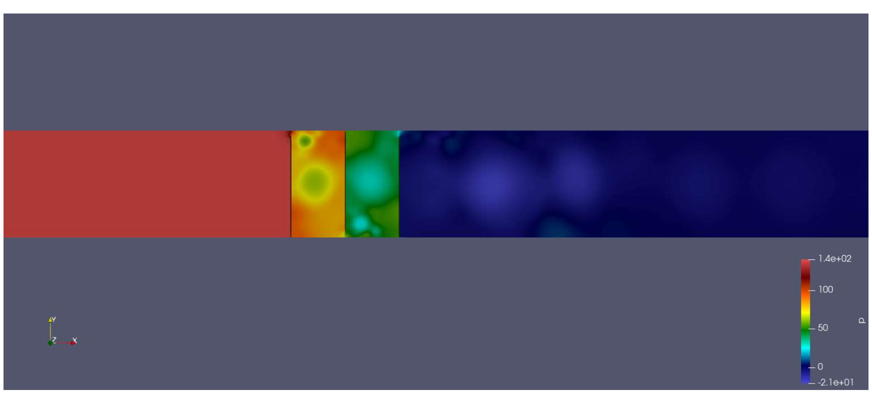

Figure 16 – Pressure contour, multi-obstacle array, Re = 200 (t = 0.033 s)

Time history graphs (Figures 17-18):

At Re=200, the time history plot for flow rate shows oscillatory behaviour, with the oscillation amplitude increasing over time and becoming periodic after t ≈ 0.04 s. The amplitude of these oscillations is greater than those observed in the previous case where there was only one obstacle present, since this means there is more vortex shedding due to multiple wakes. The mean pressure drop becomes constant at around 1.5×10^5 Pa and remains oscillatory. These values for the mean pressure drop are significantly greater than those predicted by linear Hagen-Poiseuille theory.

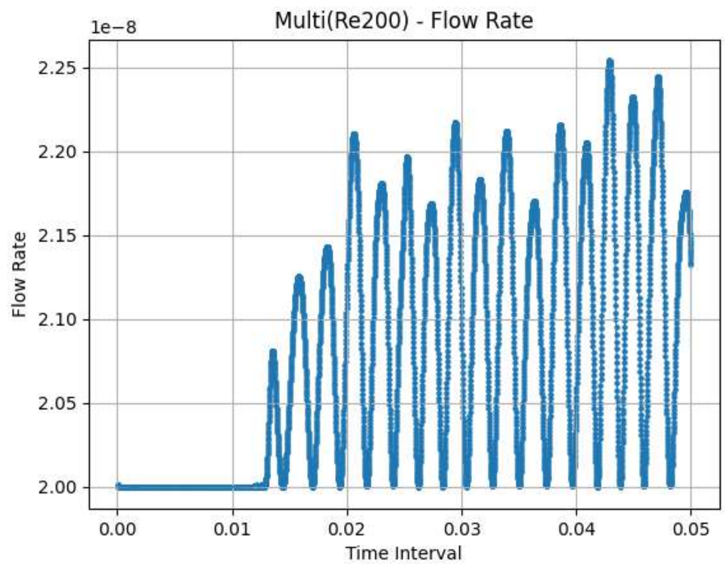

Figure 17 – Flow rate vs. time interval, multi-obstacle, Re = 200

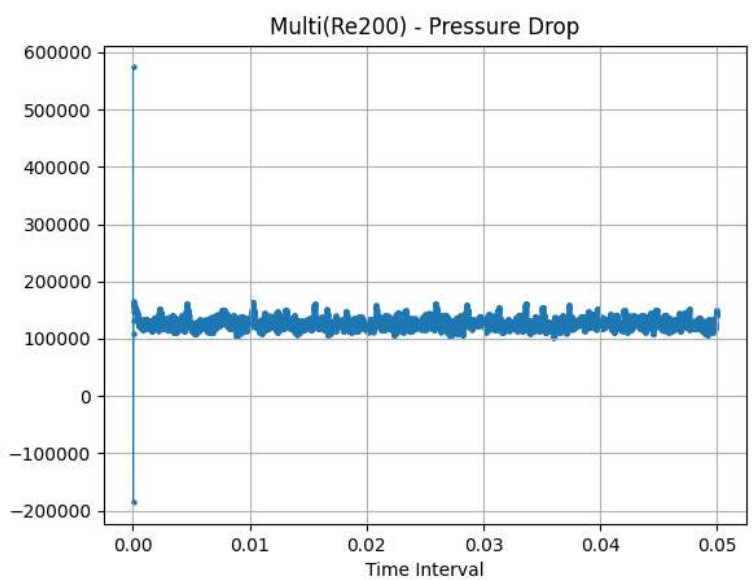

Figure 18 – Pressure drops vs. time interval, multi-obstacle, Re = 200

Table 5 – Summary of mean flow rate and pressure drop across all cases

Case	Re	Config.	Mean Q [m³/s per m]	Mean ΔP [Pa]
1	0.1	Single obstacle	$\sim 8 \times 10^{-15}$	~0.002
2	200	Single obstacle	$\sim 2.1 \times 10^{-8}$	$\sim 5 \times 10^{4}$
3	0.1	Multi-obstacle	$\sim 7 \times 10^{-15}$	~0.005
4	200	Multi-obstacle	$\sim 2.1 \times 10^{-8}$	$\sim 1.5 \times 10^{5}$

7. Discussion and Conclusion

7.1 Summary of Findings

Simulations using icoFoam transient model for the flow of liquid within microchannels with obstacles in the form of cylinders have been performed four times at Reynolds numbers 0.1 and 200 for both single and multiple obstacle cases. The results obtained can be summarized as follows:

(i) In the case of Re = 0.1, the flow is steady, symmetrical and linear. Pressure drops as a function of channel length and number of obstacles follow an expected trend, as suggested by Hagen-Poiseuille's law.

(ii) In the case of Re = 200, inertial forces cause recirculation wakes and vortex shedding downstream of each obstacle. Flow rates and pressure drop show oscillatory behavior, characteristic of non-linear resistance, according to Forchheimer laws.

(iii) Multiple obstacle channel flow at Re = 200 has a considerably higher pressure drop compared to that of the single obstacle case, showing sub-linear dependence on the number of obstacles, as predicted by the Forchheimer model due to wake-obstacle interactions.

7.2 Limitations of the Study

This current investigation involves 2D simulations only; hence, three-dimensional phenomena are ignored due to the finite thickness of the actual microchannel walls. There was no mesh-independence study carried out in this stage. A duration of 0.05 seconds in the simulation is enough for capturing the initial onset of vortex shedding, although it might not be sufficient for obtaining a fully developed limit cycle at Re = 200 involving multiple obstacles.

7.3 Future Work

The main objective of the upcoming simulation stage will be to develop and carry out steady state simulations using simpleFoam on the H-channel system, where the channel with multiple obstacles is embedded into an outlet branch. Parametric sweep of inlet pressure will be used to demonstrate flow switching and to prove that Braess's paradox takes place. The current research will also consider 3D meshing as well as impact of channel depth. Additionally, mesh independence studies will be done for both configurations of the channel.

8. Appendix

This appendix provides additional velocity contour results for completeness.

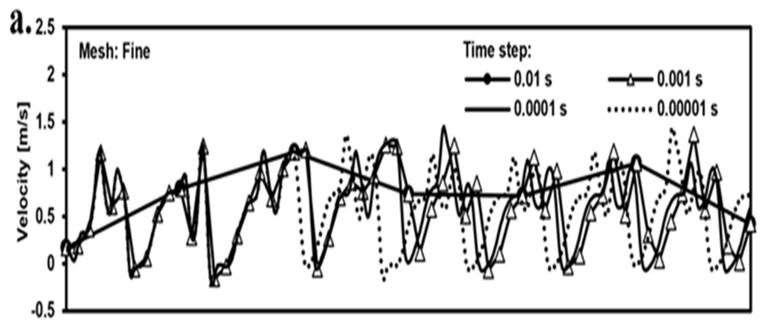

Appendix A – Transient velocity plots at different time step sizes (Re = 0.1), reproduced from Deekshith K. (2025) for reference validation

References

Case, D. J., Liu, Y., Kiss, I. Z., Angilella, J.-R., & Motter, A. E. (2019). Braess's paradox and programmable behaviour in microfluidic networks. Nature, 574(7780), 647–652. https://doi.org/10.1038/s41586-019-1701-6

Deekshith, K. (2025). Design of microfluidic networks with application to robust chemical gradient generation and passive flow control [Doctoral thesis, Indian Institute of Technology Bombay].

OpenFOAM Foundation. (2023). OpenFOAM v2412 User Guide. https://www.openfoam.com

Braess, D., Nagurney, A., & Wakolbinger, T. (2005). On a paradox of traffic planning. Transportation Science, 39(4), 446–450.

Rojas, S., & Koplik, J. (1998). Nonlinear flow in porous media. Physical Review E, 58(4), 4776–4782.